Label-free *in situ* approach for characterizing the macromolecular composition and water content in biomolecular condensates

E. Sabri[1], A. Mangiarotti[1,2,3], C. Schmitt[1] and R. Dimova[1]

[1]*Max Planck Institute of Colloids and Interfaces, Science Park Golm, 14476 Potsdam, Germany.*
[2]*Centro de Investigaciones en Química Biológica de Córdoba (CIQUIBIC), CONICET, X5000HUA Córdoba, Argentina.*
[3]*Departamento de Química Biológica Ranwel Caputto, Facultad de Ciencias Químicas, Universidad Nacional de Córdoba, X5000HUA Córdoba, Argentina.*

ABSTRACT

Biomolecular condensates are cellular organelles that form via liquid–liquid phase separation of proteins and nucleic acids. The functional role of intracelular condensates is known to be tightly coupled to material properties such as viscosity and hydrophobicity, which act as phenomenological markers of cellular state in health and disease. In turn, the material properties of condensates essentially depend on their macromolecular composition and water content. Yet, available approaches for determining condensate composition systematically involve invasive processes that often result in the destruction of the tested sample. Here, we use Raman spectroscopy coupled with spectral phasor analysis, and develop an *in situ* and label-free approach that allows to resolve molecular concentrations of any chemical species within aqueous polymer solutions and biomolecular condensates. In addition to quantifying the protein-to-water volume ratio, our method allows to quantify the degree of client molecule partitioning inside condensates. We show that water hydrogen bonding resulting from protein hydration can be quantified via this approach, and find that the overwhelming proportion of water molecules within condensates largely retain their bulk-like properties. Lastly, by coupling our characterization approach with environment-sensitive fluorescent dyes we investigate the molecular origin of condensate hydrophobicity. Our results show that the hydrophobicity of condensates is by a combination of the presence of structural motifs in the backbone of polymers constituting the scaffold, and the degree of water partitioning inside condensates.

INTRODUCTION

Biomolecular condensates form via the self-assembly of proteins and/or nucleic acids, a process known as liquid–liquid phase separation (LLPS). These protein-rich aqueous droplets act in cells as function-specific membraneless organelles that can selectively encapsulate small molecules[1, 2], modulate the rate of chemical reactions[1, 3] and participate in gene regulation[4] to mention a few. Biomolecular condensates can transition from their liquid state to gel-like or solid assemblies with significantly different material properties which act as sensitive markers of their physiological state in health and disease[5-8]. The material properties of condensates are commonly interpreted as emergent properties, governed by the structural features of biopolymers composing condensates' scaffold [5, 8-10]. Alternatively, water is known to play a dual role in cellular organization. It shapes protein structure[11-14] and biochemical activity[15], while hydrated proteins, in turn, alter the dynamics of their surrounding water shells, yielding fundamentally different properties from bulk water[9, 15]. In this context, the dynamics of water molecules are known to be entropically penalized in crowded biomolecular environments [16-19]. LLPS allows cells to reversibly reorganize intracellular water and buffer changes in cytosolic conditions, playing an essential role in maintaining cellular homeostasis under stress[9, 17]. However, the volume fractions occupied by dynamically constrained versus bulk-like water was numerically assessed as spanning up to 6 hydration layers [20-23] around protein in solution, these proportions yet remain to be experimentally determined.

Consequently, a central and unresolved question is whether the functional properties of condensates emerge from specific structural features in the protein scaffold [2, 24]—such as protein size, intrinsically disordered regions, the number of hydrophobic residues, etc.—or from the altered properties of solvent molecules inside condensate droplets compared to their bulk counterpart [1, 2]. This question becomes particularly important in understanding the molecular determinants of condensate hydrophobicity, as mounting evidence indicates that the hydrophobic properties of condensates largely govern the partitioning efficiency of small client molecules [2, 25], which has crucial implications in cellular metabolism and drug processing [26]. Nonetheless, a major limitation among the approaches available in the literature to address these questions, is that quantifying the water content within condensates, identifying the molecular constituents of their scaffolds, and measuring the partitioning efficiency of exogenous small molecules typically requires invasive and destructive steps such as sample drying [27-29], which are inherently incompatible with *in vivo* measurements.

Here, we present a combination of Raman spectroscopy and spectral phasor analysis that yields an *in situ*, label-free method allowing to quantify the respective volume fractions of polymer and water inside condensates. This approach is suitable for assessing the degree of partitioning of small molecules inside condensates, and can simultaneously quantify the fraction of hydrogen-bonded water molecules that hydrate the polymer matrix. We show that these predictions are reliable irrespective of molecular size, of the type of LLPS (i.e. associative or seggregative) and of macromolecular structural complexity. This provides a generalizable benchmark for single-droplet condensate compositional analysis. Building on this framework, we quantitatively investigate the structural properties of water molecules across all tested condensates. Last, we use ACDAN as an environment-sensitive fluorescent reporter of condensate hydrophobicity [30] to investigate how water content and the structural motifs in biopolymers correlate with the hydrophobic properties of biomolecular condensates.

RESULTS

Raman vibrational spectroscopy yields a readout of the amount of different interatomic bonds within organic compounds

Raman spectroscopy relies on inelastic photon scattering to extract information about the abundance of different types of chemical bonds in a sample, based on the vibrational modes of the bonded atoms. This technique has been widely used in biology as non-invasive probe of subtle changes intermolecular interactions, bond geometry and conformational rearrangements at the microscopic scale [31-34]. From a theoretical perspective, vibrational states of interatomic bonds can be approximated as discrete modes of a harmonic oscillator, as presented in Figure 1a, defined primarily by two parameters: the bond strength modeled by a spring constant k_{const}, and the effective mass of the bonded atoms $m_{eff} = \frac{m_1 m_2}{m_1+m_2}$, where m_1 and m_2 are the masses of the different atoms. At room temperature, thermal energy ($k_b T \sim 4.11 \times 10^{-21}$J) is typically one order of magnitude lower than the energy gap that separates the ground state from the first vibrationally excited state in organic molecules [33, 34]. This prevents intermolecular bonds from spontaneously transitioning to a vibrationally excited state.

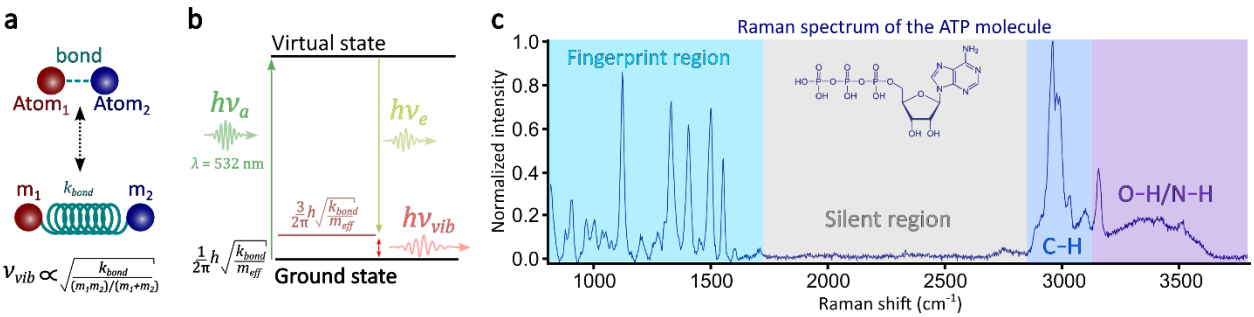

Figure 1: Illustrating the basic physical principles of Raman vibrational spectroscopy. (a) Illustration of the of an interatomic bond between two given atoms and the harmonic oscillator model in which two masses (m_1, m_2) connected by a spring of spring constant k_{bond}, to quantify the vibrational mode ν_{vib} of the oscillator. (b) Jablonsky diagram of the energy transitions involved in the inelastic Stokes-Raman effect. The red and black levels represent the vibrationally excited and ground states. (c) Normalized Raman spectrum of pure ATP as a function of the Raman shift defined as $\frac{\nu_{vib}}{c}$. The regions of the spectrum typically associated with the vibration of the CH bond, OH and NH bonds are respectively highlighted in blue and purple and are respectively located at 2800-3100cm^{-1} and 3100-3800cm^{-1} [34]. The signature region [35] highlighted in cyan, whereas the silent region [35] highlighted in grey.

The excitation of these vibrational modes is triggered by exposing a sample to a monochromatic light source [31] (Fig. 1b). The absorption of a photon triggers a transition to a virtual excited state, and the oscillator first relaxes to a vibrationally excited state. Then, it emits a second, lower-energy photon that corresponds to the vibrational frequency of the specific type of inter-atomic bond present in the sample. Fig. 1c presents the spectrum of the adenosine triphosphate (ATP) molecule as an illustrative example of the Raman spectral profile for canonical organic compounds. This figure distinguishes between spectral regions related to specific chemical features: the low frequency fingerprint region (400-1800cm^{-1}) [35] – dominated by heavy atoms linked by single- or double- covalent bonds, e.g., C–C (800cm^{-1}) and C=C (1600cm^{-1}) – whereas vibrational modes of more strongly bonded counterparts, e.g. C≡C (2160 cm^{-1}) or C≡N (2230 cm^{-1}), appear in the silent region (Fig. 1c) [35]. Interatomic vibrational modes involving lighter atom couples containing one

hydrogen atom typically appear at higher frequencies such as 2700-3100cm^{-1} for C–H [34], 3100-3800cm^{-1} for O–H [34] and 3100-3400cm^{-1} for N–H [36].

Commonly, Raman spectroscopy studies on biological and bio-mimetic materials consist in comparing changes in intensity profiles over specific spectral regions among different samples, and correlate microscopic changes in chemical and structural features to macroscopic changes in biophysical properties [33-35]. Most often, changes are quantified either in terms of ratiometric quantities at specific wavelengths [34, 37-40], shifts in local spectral maxima [33, 34, 37], or based on multi-Gaussian fit analysis of multimodal profiles [32, 37, 41]. While these approaches allow to quantify changes on arbitrary scales, their interpretation in terms of quantitative and physically relevant metrics becomes cumbersome. First, we focus on ratios of integrated signals over well-defined spectral regions in order to quantify the amount of specific bonds in a given sample.

As a proof of principle, Figure 2 presents how the relative abundance of C–H, O–H, and N–H bonds can be directly quantified from the integrated Raman intensities over the spectral regions that correspond to their vibrational modes.

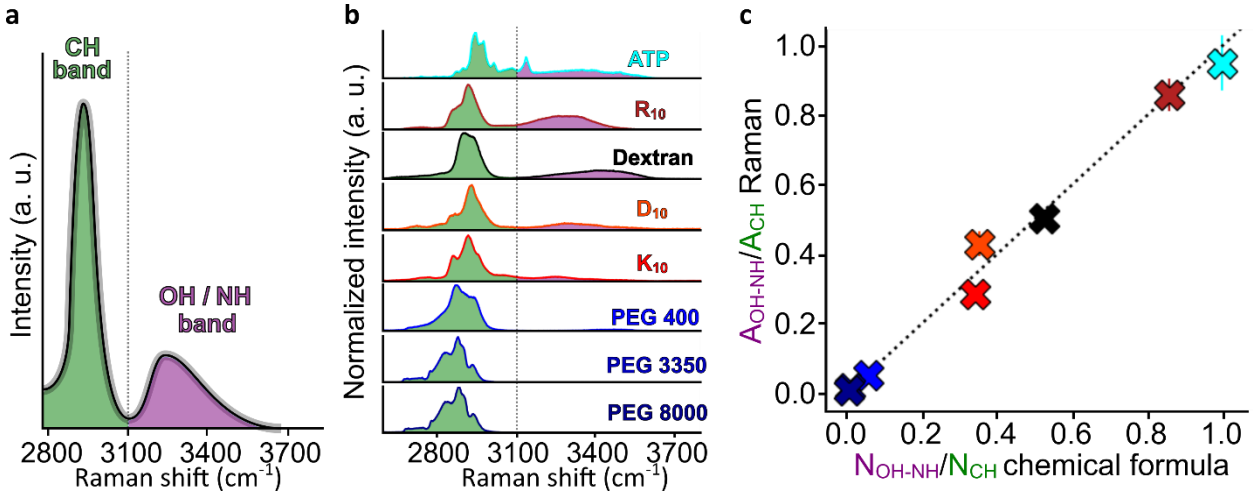

Figure 2: Raman spectroscopy enables to probe the fraction of a given type of interatomic bonds in polymers. (a) Illustration of the typical shape of the Raman spectrum of the different molecules used in this study. The areas below the curve covering the CH bond vibration region are highlighted in green and that of the OH bond and NH bond vibrations are highlighted in purple; these areas are noted A_{CH} and A_{OH-NH} respectively. (b) Normalized Raman spectra for different molecules of which the chemical formula and interatomic bonds are well known. (c) Comparing the ratio of the areas A_{CH} and A_{OH-NH} with the ratio of the known number of CH bonds over the sum of OH and NH bonds for each molecule considered in (b).

Figure 2a shows an illustration of the typical spectral profile of a protein with C–H stretching modes quantified from the area below the curve over the 2700–3100 cm^{-1} region [34] noted A_{CH}, whereas O–H and N–H stretching modes are quantified from the area below the curve over the 3100–3800 cm^{-1} region [34, 36] noted A_{OH-NH}. The chemical formulas of all compounds are known a priori. We denote the number of C–H bonds as N_{CH} and that of the combined O–H and N–H bonds as N_{OH-NH}. Figure 2b presents the normalized Raman spectral profile of the polymers and biomolecules introduced over the 2700–3800 cm^{-1} region, ordered by decreasing O–H/N–H bond abundance from top to bottom. Interestingly, Figure 2b shows that for some compounds, the

intrinsic O–H/N–H Raman signals overlaps with the spectral region often associated with pure water [39, 41]. This suggests that shape alterations of the 3100–3800 cm^{-1} spectral region in protein-rich environments could be explained as contributions, not only from water coordination through enhanced hydrogen bonding, but also based on the intrinsic composition of the protein backbone. Figure 2c compares the relative amount of C–H versus O–H and N–H bonds estimated based on the ratio of the areas below the curve (vertical axis) with that estimated from the known chemical formula of the polymers (horizontal axis). This figure clearly demonstrates that the tested ratios of integrated spectral intensities over the relevant intervals linearly correlates with the stoichiometric ratios across all tested molecules. This provides a quantitative basis for estimating the relative density of distinct bond types within crowded biomolecular environments.

Raman spectral phasor representation quantifies the fractional composition of polymers and water in crowded macromolecular solutions undergoing LLPS

Over the past few years, Raman spectroscopy has gained momentum in the field of biomolecular condensates [42], with a particular emphasis on its ability to resolve LLPS propensity markers within protein structure [37, 43], identify cellular markers of LLPS-mediated stress response [33, 39], and more recently, understanding the role of water dynamics in the macroscopic-scale properties of condensates [38, 39, 41, 44]. In this latter context, special attention has been given to probing changes in the intensity profile of the O–H bond stretching band (3100-3800cm^{-1}), where altered spectral profiles are commonly interpreted as variations in hydration levels an water dynamics relative to protein or nucleic acid content through hydrogen bonding [38, 41, 44]. While these studies put forward the potential of Raman spectroscopy to investigate water dynamics at a subcellular scale, the role of the protein backbone has largely been overlooked in the interpretation of experimental results.

To address this issue, we took advantage of Fourier transform properties to investigate how the above results can be extended to probe the volume fractions of water and proteins/polymers in different phase separated systems.

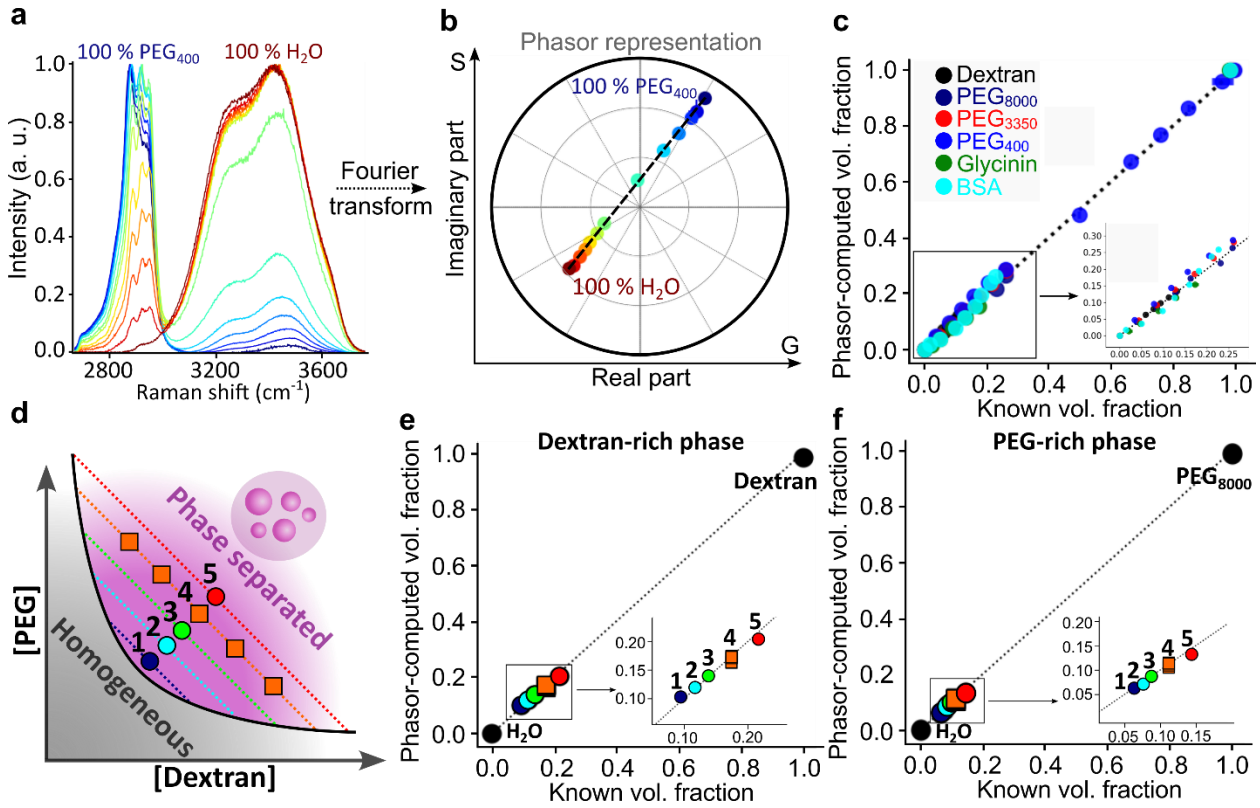

Figure 3: Phasor analysis enables a direct quantification of the volume fraction occupied by macromolecules in aqueous solutions and phase separated systems. (a) Raman spectra of PEG_{400}-H_2O mixtures, the different colors from red to blue represent conditions with 100%, 92.7%, 83.5%, 74.2%, 64.9%, 46.4%, 27.8%, 23.2%, 18.5%, 13.9%, 9.3%, 4.6% and 0% PEG_{400} content respectively. (b) Phasor representation of the spectra in (a). The black dotted line is a guide to the eye. (c) Comparing the macromolecule volume fractions computed based on the phasor representation presented in (b), following Eq. (M8), with the experimentally controlled volume fraction of polymers in aqueous solutions. The inset shows a zoomed-in representation of this comparison. The black dotted line is a guide to the eye confirming that the phasor approach based on Eq. (M8) systematically provides an accurate readout of polymer-to-water ratio. (d) Schematic representation of the phase diagram of a PEG-dextran mixture inspired from ref [45]. The purple and dark grey regions of the diagram respectively represent the PEG-dextran concentration conditions for which the solution undergoes LLPS or is homogeneous; the colored dotted lines represent different tie lines and the black straight line is the binodal. The different colors (e) Comparing the phasor-computed volume fractions of dextran in the dextran-rich phases of phase separated solutions with that of the dextran volume fraction reported in ref. [45]. The inset shows a zoomed-in representation of this comparison. The numbers 1-5 correspond to arbitrary indices used to discriminated between the different tie lines explored in this study as showed in panel (d). (f) Similar to (e) for the volume fraction of PEG in the PEG-rich phase.

First, we use aqueous binary mixtures of PEG as a well-characterized and affordable water-soluble polymer system. We choose the 2700-3800 cm^{-1} spectral region as a reference to characterize the polymer-to-water volume fraction at different PEG_{400} volume ratios, of which the Raman spectra are presented in Fig. 3a. Figure 3b presents the associated phasor space representation (see methods and Fig. S1), where vertical and horizontal phasor coordinates respectively correspond to the real (G) and imaginary (S) components of the Fourier transform of the Raman spectra [46] (detailed definitions are provided in the methods section), providing an optimized formalism for the geometric determination of a mixture's fractional composition (see Fig. S1). Figure 3b shows that the pointwise phasor representation of the spectrum of all aqueous water-PEG_{400} mixtures fall onto the straight line connecting the two pure compounds (i.e. water and PEG_{400}), consistent with

the linearity of phasor-space geometric operations in binary mixtures [46]. Figures S2, S11 show that this principle generalizes across all tested polymer/protein–water systems. Next, we take advantage of the properties of phasors (see Fig. S1 and methods) and benchmark this approach in Fig. 3c for a broad set of compounds, demonstrating that the volume fraction V_{phasor} (see methods) polymer occupy in aqueous solution can be precisely determined based on their spectral phasor representation (see Figs. S1, S2, S11). The phasor-derived expression represented on the vertical axis is compared with the known volume fraction of polymer V_{known} used to prepare the solutions. The latter values were obtained using the relation $V_{known} = \frac{w_{frac}\, v_p}{v_p\, w_{frac} + (1 - w_{frac})\, v_{H_2O}}$, where w_{frac} represents the chosen weight fraction of the polymer in the mixture, v_p represents the specific volume of the polymer, and v_{H_2O} the specific volume of water. The values of all parameters used in this study are listed in Table S1.

Next, we extend this approach to biomolecular condensates. Figure 3d schematizes the generic phase diagram underlying the LLPS of the aqueous two-phase system formed by PEG and dextran polymers mixtures inspired from ref. [45]. The polymer concentration in each of the two polymer-rich phases can be retrieved from the initial polymer concentrations (colored dots and squares) and the intersection of their respective tie lines (dotted colored lines) with the binodal (straight black line). Figures 3e,f show the volume fraction occupied by polymers in the PEG-rich (Fig. 3e) and dextran-rich phase (Fig. 3f) computed via the present phasor approach (vertical axis) for different tie lines, compared with volume fractions obtained by optical refractometry measurements reported in ref. [45] (horizontal axis).

This strong agreement demonstrates that our method scales reliably with the fractional composition of phase-separated systems, enabling the extension of our Raman spectral phasor analysis to single-droplet measurements presented in Fig. 4.

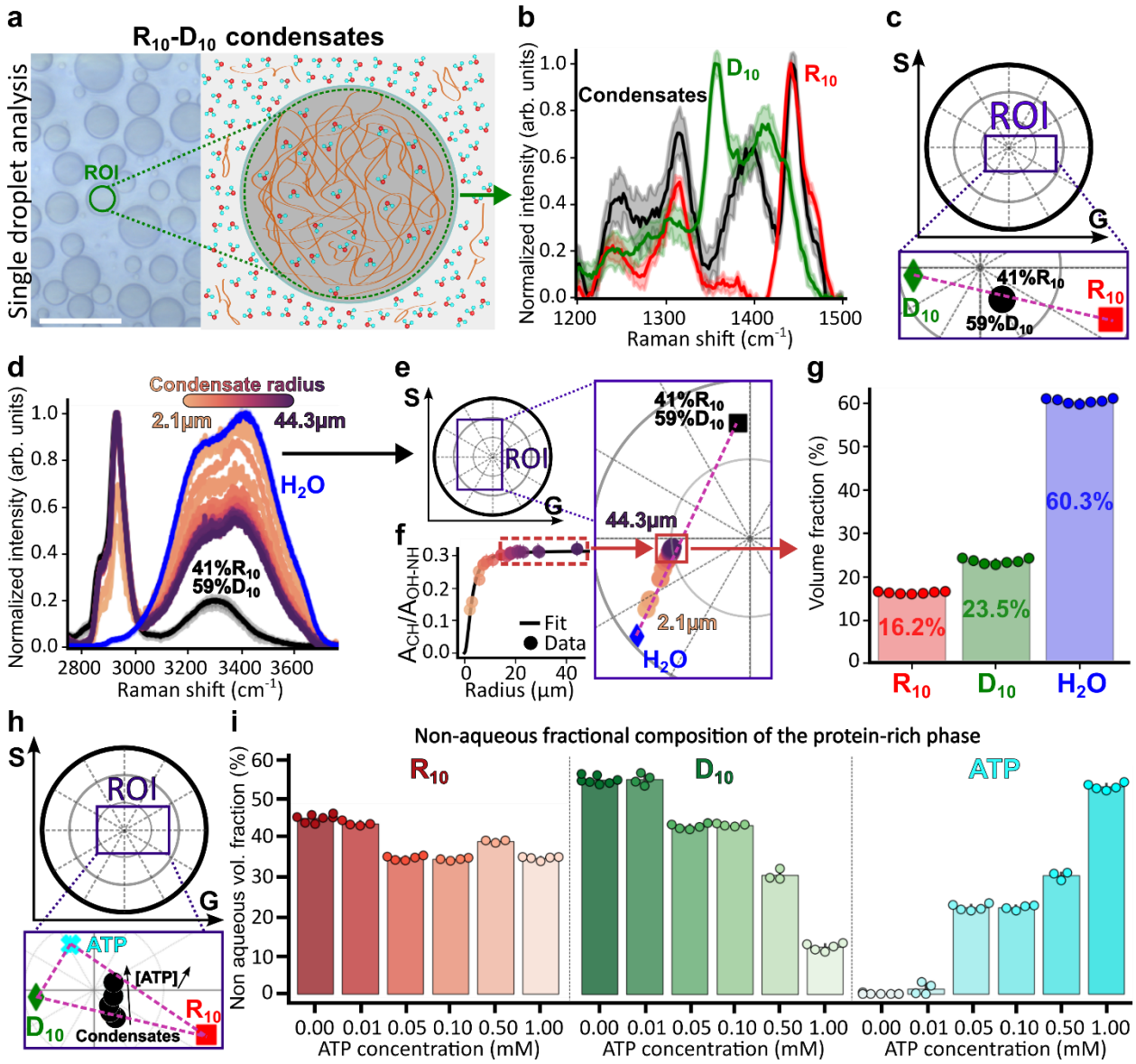

Figure 4: Single droplet phasor analysis of Raman spectrum enables a full characterization of condensate composition. (a) Left: bright field snapshot of an R_{10}-D_{10} condensate sample, droplets were obtained by mixing two aqueous polypeptide solutions to obtain a final concentration of 2.5mM R_{10} and 2.5 mM D_{10}. The region of interest (ROI) noted in green corresponds to the acquisition zone within which the Raman signal is collected. The scale bar is 40µm. Right: Illustration of the protein-rich and protein-depleted phases of a condensate system. The dense region represents the region of interest of this figure. (b) Normalized Raman intensity over the 1250-1500 cm^{-1} portion of the signature region. The red, green and black curves correspond to the Raman spectra of pure R_{10}, pure D_{10} (see Fig. 2c) and R_{10}-D_{10} condensates represented in (a). Shaded regions correspond to their respective measurement error (n = 17). (c) Phasor representation of the different Raman spectra, the color of each point corresponds to that of its Raman spectrum counterpart. The proportions of R_{10} and D_{10} were computed based on Eq. (M8). (d) Normalized Raman intensity over the CH and OH vibration bands (2700cm^{-1}-3800cm^{-1}). The blue and black curves respectively represent the Raman spectra of pure water and a weighed sum of the spectra of pure R_{10} and pure D_{10}. The colored straight lines represent the Raman spectra of condensates of different radii of which the magnitude can be assessed from the color bar. (e) phasor representation of the data in (d), the dotted line is a guide to the eye that attests of the alignment of the datapoints. The color of each data point corresponds to that of its Raman spectrum counterpart presented in (d). The dotted line in cyan is a guide to the eye connecting the water and protein signals. (f) Ratio of the area below the Raman curves of condensates over the CH bond vibration region (2700-3100cm^{-1}) noted A_{CH} and OH and NH bonds vibration region (3100-3800cm^{-1}) noted $A_{OH\text{-}NH}$ as a function of condensate radius. The color of the data points relates to the

radii of the different condensates considered and is the same as in (d-e). The function used to fit the data was of the type $y = aR^2/(R^2 + b)$, where R represents condensate radius and a and b are fitting constants. The dotted rectangle represents the set of datapoints for which the ratio $A_{CH}/A_{OH\text{-}NH}$ no longer depends on condensate radius. (g) Volume fractions of the different components of the dense phase of R_{10}-D_{10} condensates. The dataset (n=7) is a truncated version of the data presented in (d-f) where all kept datapoints have a $A_{CH}/A_{OH\text{-}NH}$ ratio within a 1% error interval with respect to the maximum value of the fit presented in (f). (h) Phasor representation of the different Raman spectra of condensates with different initial concentrations of ATP (0mM, 0.01mM, 0.05mM, 0.1mM, 0.5mM and 1mM represented by black dots). The proportions of R_{10}, D_{10} and ATP were computed based on Eqs. (M8-M10). (i) Molecular composition of the protein-dense phase of R_{10}-D_{10} condensates at different ATP concentrations. The total concentration in peptides was kept constant at 2.5mM while the final concentration in ATP was set to 0mM (n = 7), 0.01mM (n = 4), 0.05mM (n = 5), 0.1mM (n = 4), 0.5mM (n = 3) and 1mM (n = 5).

As an initial step, we examined the dense phase of a condensate system formed by oppositely charged polypeptides R_{10} and D_{10} represented in Fig. 4a. Focusing on a low-frequency spectral signature region where R_{10} and D_{10} exhibit distinct profiles and over which the water signal is negligible, we applied the same phasor-space approach but taking the 1290-1470cm^{-1} spectral interval to define phasor space boundaries (see methods) to disentangle the spectral contributions of each polypeptide (Fig. 4b,c). This revealed an asymmetry of 41% positively charged R10 and 59% negatively charged D10 in the dense phase, consistent with the intrinsic negative zeta potential of R_{10}-D_{10} condensates [47].

We next analyzed Raman spectra across the full 2800–3800 cm^{-1} region for condensates of different radii (Fig. 4d). These measurements revealed a strong dependence of the O–H band intensity on droplet size for condensates of radii below 10µm, suggesting an increase in the Raman signal of external water with decreased condensate size. Small condensates, although appearing to fill the projected focal area of the ROI (Fig. 4a), do not fully occupy the vertical extent of the acquisition zone (~5µm) which artificially enhances the water signal (see Fig. S3). As a result, the phasor signature of smaller condensates tends to shift closer to that of bulk water (Fig. 4e). Above a radius of ~10-15µm, this dependence vanishes as the acquisition zone becomes gradually saturated in condensate material (see Fig. S3) enforcing a vertical asymptote onto the sampled protein-to-water ratio represented by the variable A_{CH}/A_{OH-NH} (Fig. 4f). We used this size threshold as a cutoff radius beyond which the water composition was assumed stable and for which an exhaustive characterization could be performed as presented in Fig. 4g. Notably, Figs. S5-S9 present similar analyses for all types of phase separating systems tested in this study. Additionally, because of its ability to resolve the polymer-to-water ratio in both the dense and dilutes phases, this approach can in principle be employed to resolve tie lines in any phase separating system.

Next, we investigate the influence of ATP addition, a small molecule known for its physiologically multifunctional intracellular role[48, 49], on the composition of the dense phase. Figure 4h shows that upon the addition of ATP upon condensate formation the spectral phasor profile of condensates of R_{10}-D_{10} starts to drift away from the straight line connecting the pure R_{10} and D_{10} compounds. Based on similar geometric rules detailed in Fig. S1, Fig. 4h shows that the proportions of both the polypeptides and the ATP that partitions inside the dense phase can be quantified based on the shift of the condensate spectral signatures towards the ATP reference point. Fig. 4i shows that ATP partitioning inside the droplet can reach a molecular fraction as high as 50% of the dense phase content at a 1 mM total ATP concentration, and that despite the constant polypeptide concentrations of 2.5 mM R_{10} and D_{10}. While R_{10} levels varied only modestly (<10%) upon ATP

addition, whereas D_{10} content decreased dramatically—by ~40 percentage points—demonstrating preferential replacement of the acidic polypeptides by the negatively charged ATP.

Raman hyperspectral imaging and phasor analysis provide a spatially resolved map of micro-heterogeneous system composition

Fig. 5 presents how this quantitative framework can be extended to perform hyperspectral imaging for mapping the fractional composition of biomolecular condensates.

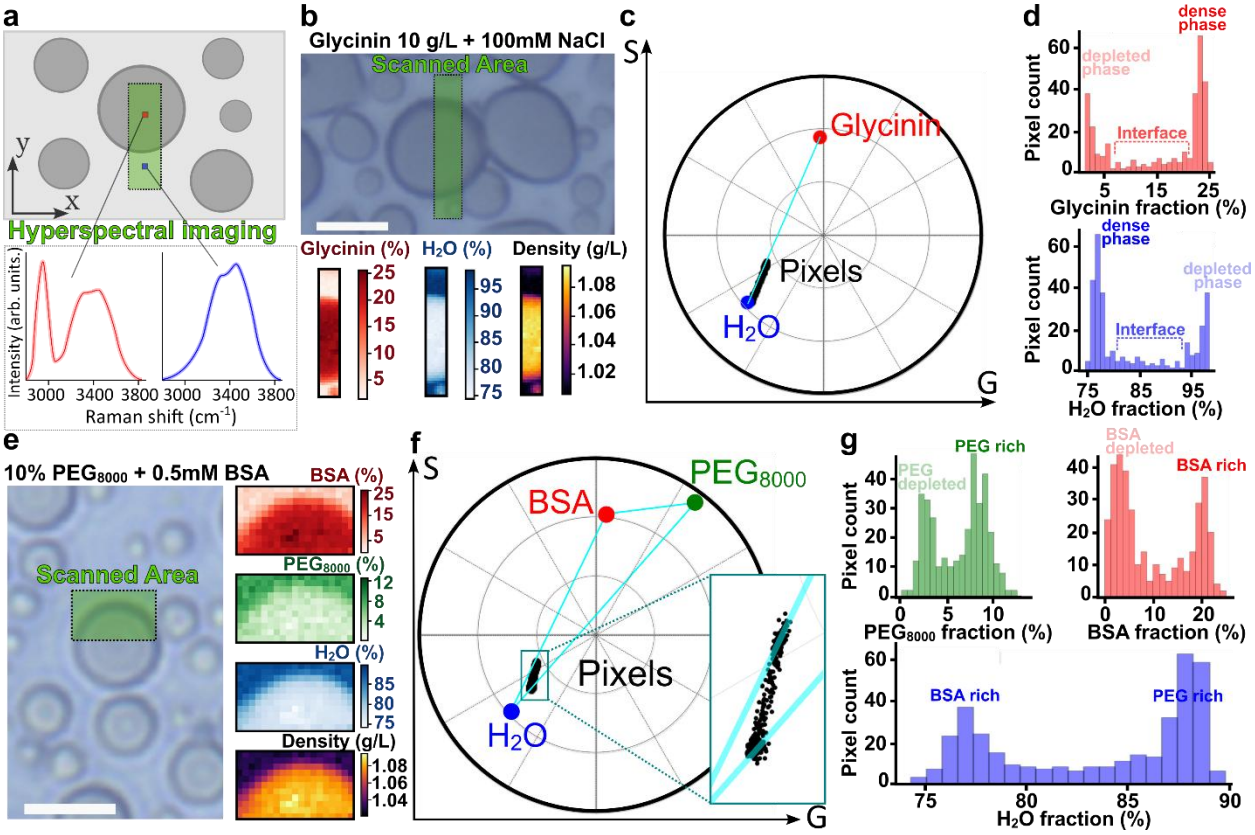

Figure 5: Hyperspectral imaging of biomolecular condensates allows mapping the volume fraction occupied by their constituents. (a) Schematic illustration of Raman-based 2D confocal microscopy hyperspectral imaging of a biomolecular condensate sample. The top panel illustrates the 2D cross section of a condensate sample. Dark grey and light grey domains represent the protein-rich and protein-depleted regions respectively. The red and blue curves of the bottom panel illustrate the expected shape of the Raman spectra respectively sampled in the protein-rich and protein-depleted regions. (b) Top panel: bright field snapshot of a glycinin condensate sample, droplets were obtained by mixing two solutions of glycinin and NaCl to the final indicated concentrations. The scanned region of interest is highlighted in green. The scale bar represents 10µm. Bottom panel: maps of the volume fraction occupied by the glycinin (left panel in red) and water (middle panel in blue). The density (right panel) was mapped based on the specific volume of each component and using Eq. (M8). (c) Phasor representation of the spectral data contained in each analyzed pixel (black dots) of the scanned area in (b) sampled over the 2700-3800cm^{-1} spectral region. The red and blue dots respectively represent the spectra of pure glycinin and pure water on the phasor plot, the straight line in cyan is a guide to the eye connecting these two points. The alignment of the pixel spectral data onto this line attests of the purely binary composition (i.e. glycinin and bulk-like water) of the scanned sample. (d) Histograms of the volume fraction occupied by glycinin (top panel) and water (bottom panel) for all the pixels in the scanned area in (b). (e) Left panel: bright field snapshot of a PEG-BSA condensate sample. Droplets were obtained by mixing two aqueous solutions of PEG 8000 kDa and BSA buffered in PBS to the indicated final concentrations. The scanned region of interest is highlighted in green. The scale bar represents 10µm. Volume fractions of BSA, PEG_{8000} and water are respectively mapped in red, green and blue. The density (right panel) was mapped based on the specific volume of

each component and using Eqs. (M8-M10). (f) Phasor representation of the spectral data contained in each analyzed pixel (black dots) of the scanned area in (e), sampled over the 2700-3800cm^{-1} spectral region. The red, green and blue dots respectively represent the spectra of pure BSA, pure PEG_{8000} and pure water on the phasor plot, the straight lines in cyan are guides to the eye connecting these three points. (g) Histograms of the volume fraction occupied by PEG_{8000} (top left panel), BSA (top right panel) and water (bottom panel) for all the pixels in the scanned area in (e).

Figures 5a,b shows that Raman hyperspectral imaging, (i.e. spectra acquired pixel by pixel) can be used to map the fractional composition of glycinin protein and water inside glycinin condensates, across the dense and dilute phases, based on the same approach as that presented in Figs. 3-4. The lower panel of Fig. 5b also shows that knowing the volume fractions occupied by the protein and water along with their specific volume (glycinin ~ 0.73 L/g, water ~ 1 L/g), the sample density can be mapped down to pixel resolution, provided that the specific volumes typically obey the conservation relation $\frac{1}{\rho_{tot}} = \frac{w_{H_2O}}{\rho_{H_2O}} + \frac{w_{glycinin}}{\rho_{glycinin}}$ at these concentrations [45], where ρ_{tot} is the pixel resolved total density and ρ_i and w_i respectively correspond to the density and weight fraction of the i-th compound. In Fig. 5c, the phasor representation of spectra from all pixels in Fig. 5b aligns along the water–glycinin segment, confirming that the system is a strictly binary mixture of water and glycinin in varying proportions.

Interestingly, the alignment observed suggests that the spectral features associated with long-lived hydrogen-bonded water molecules only contribute to a negligible extent to the overall spectral properties of the water inside the dense phase (see Fig. S11). Figure 5d provides statistical distributions of pixel intensities around the respective water and glycinin volume fractions from which dense (~23% glycinin and ~77% water) and dilute (~2% glycinin and ~98% water) phases can be clearly distinguished. Extending Raman-based fractional mapping to a ternary mixture (BSA, PEG, water; Fig. 5e), clearly shows that BSA concentrates within the dense phase, whereas PEG accumulates in the surrounding more hydrated phase. The corresponding phasor plot (Fig. 5f) shows that all pixel spectra lie within the triangle spanned by pure PEG, BSA and water, consistent with ternary mixing. Fig. 5g reports the pixel-level volume fraction statistics for PEG, BSA and water, where dense and dilute phases are clearly distinguished: PEG peaks at ~2.5% (dense) and ~8% (dilute), BSA at ~20% (dense) and ~4% (dilute), and water at ~77.5% (dense) and ~88% (dilute).

Combining Raman spectral phasors with environment-sensitive dyes reveals the compositional determinants of condensate hydrophobicity

Here we compare the water-to-protein volume fractions obtained from the Raman spectral analysis presented in the previous sections, to the hydrophobicity of biomolecular condensates, quantified on a scale of dielectric constant. While the technical details of the latter analysis are presented in ref. [30], Figs. 6a,b briefly summarize the approach.

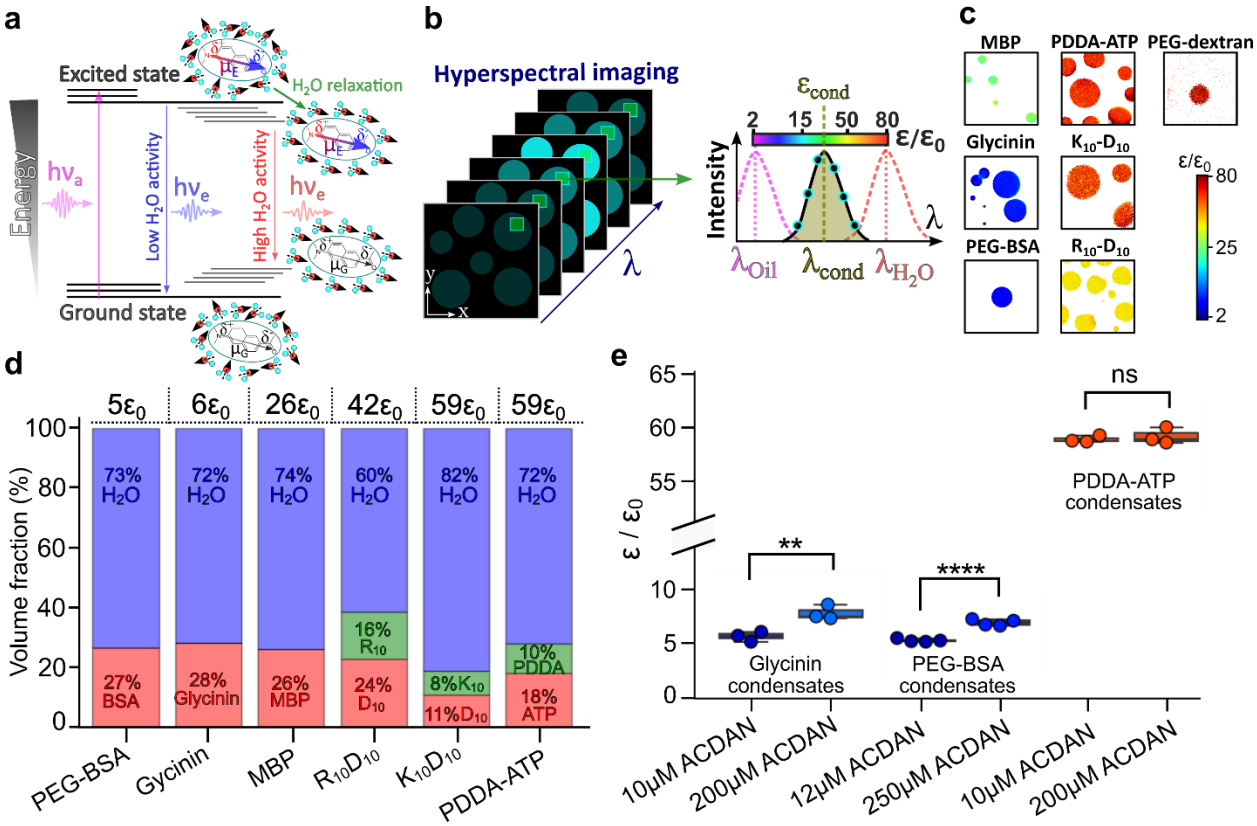

Figure 6: Fluorescence-based measurements of water dipolar relaxation unveils the complex origin of hydrophobicity of biomolecular condensates. (a) Perrin-Jablonsky diagram illustrating the dependence of ACDAN fluorescence on water dipolar relaxation. The molecular structure of ACDAN and schematic illustration of its dipole moment change are depicted in the sketches. Non-relaxed water dipoles cause a weak red shift of the dye fluorescence, while relaxed water dipoles lead to a strong red shift in the dye fluorescence. (b) Schematic representation of fluorescence-based 2D confocal microscopy hyperspectral imaging of a biomolecular condensate sample. The local permittivity in a pixel of the image (either for the dense or dilute phases) is determined based on a prior calibration with a panel of different solvents of known dielectric constant, see ref [30] for details. (c) Mapping the dielectric constant of different condensate systems. The color bar represents the dielectric constant normalized by the permittivity of vacuum ϵ_0. (d) Representing the volume fraction of proteins and water constituting the protein-dense phase of different biomolecular condensate systems. The dielectric constant indicated on the top of each bar plot was calculated by taking the average values over all the pixels in the images presented in (c). (e) Comparing the computed dielectric constant at low versus high concentrations of the ACDAN probe. Here the number of stars correspond to the negative power of 10 associated with the p-value of the student test used for the statistical analysis of the data.

Fig. 6a presents a Perrin-Jablonsky illustrating the conventional understanding [16, 18, 19] of the dependence of ACDAN fluorescence on the dipolar relaxation within its immediate environment, i.e. where emission redshift happens as a consequence of water dipolar relaxation. In this narrative, water molecules in the dense phase interact with the densely packed proteins forming the condensate scaffold resulting in either slower dipolar relaxation [16, 18, 19], suppressed dipolar relaxation by hydrogen bonding [41, 50, 51], or both [52, 53]. While our results presented below challenge the role of hydrogen bonding in this narrative, which is further discussed in the next section.

Using fluorescence-based hyperspectral imaging approach calibrated with the ACDAN dye and presented in details in ref. [30], we determined the dielectric properties of the dense phase of condensates as illustrated in Fig. 6b, revealing a broad continuum of hydrophobicity across condensates formed via LLPS of distinct types (Fig. 6c). While the ACDAN dye was chosen for

its robust and broadband dielectric measurement characteristics [30], Fig. S10 shows that these trends are well reproduced by the emission redshift of Nile red, another well-known environment-sensitive fluorescent reporter [54], underscoring the universal character of this classification.

Fig. 6d presents the fractional composition of condensates with decreasing hydrophobicity from left to right. Remarkably, while Fig. 6d shows that in condensates made of short and unstructured oppositely charged polypeptides with highly similar electrostatic-based LLPS origin (e.g. R_{10}-D_{10} versus K_{10}-D_{10} condensates), the increase of the volume fraction occupied by water is highly correlated to that of the dielectric constant reported via ACDAN fluorescence. Interestingly, for condensates whose scaffold is composed of much larger molecules exhibit more extreme degrees of dipolar relaxation—glycinin, BSA, and MBP having the highest apparent hydrophobicity and PDDA-ATP condensates appear highly hydrophilic (see Fig. 6d)—all display a high water content (> 72%, see Fig. 6d) consistent with values reported in the literature[27, 55]. However, water partitioning alone cannot account for the broadness of fluorescently measured values of condensate dielectric constants presented in Figs. 6c and S10. Additionally, Figs. 5, S5-9 and S11 show that the amount of hydrogen-bonded water in the dense phase is negligible for all studied condensates samples which rules out the hypothesis of suppressed dipolar relaxation via hydrogen bonding. Importantly, the observed trends could be explained by a slowdown in water dynamics upon protein hydration, as previously evidenced experimentally by terahertz spectroscopy measurements [42, 51] and dielectric relaxation spectroscopy [52], which in turn suppresses the emission redshift of dye sensors [56].

Nevertheless, Figure 6e investigates a complementary scenario in which the ACDAN undergoes uneven distribution in condensate systems composed of large globular proteins such as BSA and glycinin, exhibiting structural patterns in their structural backbone. In this scenario, the uneven mixing would originate from the preferential partitioning of the dye in these water-depleted structural patterns. Consequently, upon dramatic increases in ACDAN concentration shown in Fig. 6e, these regions would become partially saturated, exposing the dye to higher amounts of water. This enhanced exposure would result in an increase in the measured dielectric constant, which does not occur for hydrophilic and unstructured polymer systems composing as PDDA-ATP condensates. Figure S12 further addresses how deviations from evenly mixed solutions can be quantified. Additionally, Fig. S13 investigates the influence of high ACDAN concentrations on the phase diagram of BSA and glycinin condensates. This figure shows that despite the higher apparent dielectric constant of such condensates reported in Fig. 6e, the ratio A_{CH}/A_{OH-NH} of the condensate droplets is systematically higher at higher ACDAN concentrations. This increased abundance of C–H bonds relative to O–H bonds suggests that increasing the ACDAN concentration does not enhance water partitioning inside the dense phase. These results are consistent with numerical studies of water dynamics reporting increases of water relaxation timescales by two orders of magnitude in structured regions of a protein's backbone [20-22].

DISCUSSION

The present study provides a direct means of quantifying condensate composition *in situ*, allowing to bypass the invasive steps of centrifugation and drying typically required for measuring condensate hydration levels [27, 28] and client molecule preferential partitioning [29]; steps that involve varying conditions of temperature and pressure which likely perturb the phase behaviour of the observed system. It also provides a label-free platform for precisely quantifying the partitioning of

client molecules–which can be extended to larger molecules such as RNA and DNA–lifting the requirement of tagged proteins that may affect its native topological properties, and consequently their partitioning efficiency and binding abilities [57-59]. This study demonstrates that Raman spectral phasor analysis is an efficient tool for resolving protein- and water-specific vibrational signatures with high precision at the single droplet level.

This approach also offers a crucial tool to address a long-standing biophysical question about the role of water dynamics in shaping the macroscopic properties of crowded macromolecular environments; especially on the role of hydrogen bonding in defining condensates hydrophobicity. Interestingly, the present results contrast with earlier reports claiming that the structural properties of water is sensitive to the type of LLPS (i.e. seggregative versus associative) [41], and depends on water hydrogen bonding du to interactions the protein scaffold [41]. Nevertheless, these differences can be explained by how previous studies ignored the influence of the size of condensates, which is an important factor to account for (see Figs. 4, S5-S9, S11). Additionally, previous studies also ignored the spectral contributions of the O–H and N–H bonds in the protein backbone [41]; this can be misleading when trying to interpret water dynamics based solely on the O–H vibration region of the Raman spectrum (see Fig. 2c). Interestingly, once these contributions are accounted for, deviations in the Raman spectral profile of water inside condensates vanish, aligning the spectral signature with bulk-like behavior (see Figs. 4, S5-S9, S11), even for hydrophobic condensates exhibiting low dielectric constants when probed via fluorescent methods (see Fig. 6). These results suggest that water partitioning has a much stronger influence on condensate dielectric constant than hydrogen bonding (see Fig. 6d).

Additionally, our results show that there is no general unifying principle linking the dielectric constant of condensates with the amount of water they contain nor to specific chemical features of the polymer scaffold. but a more complex combination of these two contributions. As a result, condensates could hypothetically play the role of protein hubs with dual hydrophobic properties. Highly hydrophobic small molecules could be locally enriched near structured regions while more hydrophilic small molecules could reside in the remaining 60-80% water enriched. Overall, these results pave the way towards a better understanding of the interplay between protein hydration, protein structure and condensate hydrophobicity. This becomes particularly important when investigating how dipolar relaxation contrasts between condensates and their immediate aqueous environment can affect their interfacial properties, shaping how immiscible protein-rich domains self-assemble into core-shell multifunctional compartments[4, 8, 60]. Recent work even shows that such hydrophobicity contrasts can play an important role in condensate–membrane affinity and mutual remodeling[8, 30, 38] which governs key cellular processes such as endocytosis[61] and membrane repair[62].
Overall, this approach enables robust mapping of condensate composition formed by proteins with diverse sizes, structures, and phase-separation mechanisms, offering valuable mechanistic insights for bioengineering applications, particularly relevant for tracking the compositional dynamics of biomimetic and biological systems.

METHODS

Materials

6-acetyl-2-dimethylaminonaphthalene (ACDAN) was purchased from Santa Cruz Biotechnology (USA). Polydiallyldimethylammonium chloride (PDDA, 200-350 kDa, 20 wt% solution in water), adenosine triphosphate (ATP) and sodium hydroxide (NaOH) were obtained from Sigma-Aldrich (Missouri, USA). Poly(ethylene glycol) (PEG 8000, Mw 8kg/mol and PEG 400, Mw 4kg/mol) and dextran from Leuconostoc mesenteroides (molecular weight between 400 kDa and 500 kDa) were purchased from Sigma-Aldrich. The oligopeptides, poly-L-lysine hydrochloride (degree of polymerization, n = 10; K_{10}), poly and poly-L-aspartic acid sodium salt (n = 10; D_{10}) were purchased from Alamanda Polymers (AL, USA) and used without further purification (≥95%). BSA (≥98% purity, 66kg/mol), MBP bovine (≥90%) Polyvinyl alcohol (PVA, Mw 145000kg/mol) was purchased from Merck (Darmstadt, Germany). All solutions were prepared using ultrapure water from SG water purification system (Ultrapure Integra UV plus, SG Wasseraufbereitung) with a resistivity of 18.2 MΩ cm.

Condensate formation and labelling

Coverslips for confocal microscopy (26 × 56 mm, Waldemar Knittel Glasbearbeitungs GmbH, Germany) were washed with ethanol and water, then passivated with a 40 mg/mL PVA solution and an aliquot of 10µL of condensates suspension was placed on the coverslip before imaging.

PDDA-ATP condensates: Phase separated droplets were formed by gently mixing aliquots of stock solutions of ATP and PDDA (in this order) with ACDAN in pure water to a final volume of 10 µL. The final concentration of each component was as follows: 14.8 mM ATP, 4.9 mM PDDA, 10µM ACDAN.

Glycinin condensates: Freeze-dried glycinin was a gift from Dr. Nannan Chen. The purification is detailed in ref [63]. A 20 mg/mL glycinin solution at pH 7 was freshly prepared in ultrapure water and filtered with 0.45 µm filters to remove any insoluble materials. To form the condensates, the desired volume of the glycinin solution was mixed with the same volume of a NaCl solution of twice the desired final concentration. In this manner, the final protein concentration was 10 mg/mL [63]. The final concentration of ACDAN was 5µM.

K_{10}-D_{10} and R_{10}-D_{10} condensates: Phase separated droplets were formed by gently mixing aliquots of stock solutions of D_{10} and K_{10} or R_{10} (in this order) with ACDAN in pure water to a final volume of 10 µL. The final concentration of each component was as follows: 2.5 mM D_{10}, 2.5 mM K_{10} or R_{10}, 15µM ACDAN.

PEG-BSA condensates: Phase separated droplets were formed by gently mixing aliquots (via pipetting and releasing 3 times the total volume) in a 1:1 ratio of stock solutions of 20% PEG-8000 in PBS with 30µM ACDAN with BSA dissolved in PBS at half the desired concentration and to a final volume of 10 µL.

PEG-Dextran condensates: A polymer solution in composed of the desired weight fractions of PEG and dextran were prepared and left, when relevant, for 2 days to completely phase separate

and equilibrate. ACDAN was then added to each phase to reach a final concentration of 25µM of ACDAN.

MBP condensates: MBP condensates were prepared by following the procedure described in [64]. Briefly, a 5mg/mL solution of MBP dissolved in water was mixed with a 20mM NaOH solution of 10µM ACDAN in a 1:1 ratio.

Confocal microscopy and fluorescence hyperspectral imaging

Hyperspectral images were acquired using a confocal Leica SP8 FALCON microscope equipped with a 63×, 1.2 NA water immersion objective (Leica, Mannheim, Germany). The microscope was coupled to a pulsed Ti:Sapphire laser MaiTai (SpectraPhysics, USA), with a repetition rate of 80 MHz. A two-photon wavelength of 780 nm was used for ACDAN excitation. Image acquisition was performed with a frame size of 512 × 512 pixels [38, 65] and a pixel size of 72 nm×72 nm using a Hyd SMD detector in standard mode. For hyperspectral imaging, the xyλ configuration of Leica SP8 was used, sequentially measuring in 32 channels with a bandwidth of 9.75 nm in the range from 416 to 728 nm. Some hyperspectral images were realigned using the ImageJ software and all hyperspectral stacks were processed into .r64 files by the SimFCS software developed at the Laboratory of Fluorescence Dynamics (available at https://www.lfd.uci.edu/globals/), and analyzed using Python code based in the PhasorPy library (available at https://www.phasorpy.org/).

Raman confocal analysis and hyperspectral imaging

Raman images and spectra were acquired with a Raman confocal microscope Alpha300 R (WITec GmbH, Germany) with Zeiss EC Epiplan 50×/0.75 objective, at an excitation wavelength of 532 nm and 50 mW laser power. Spectra were acquired in the range 20–4100 cm^{-1}. The Raman band of the silicon wafer was used to calibrate the spectrometer. Data were analysed with the Project FIVE v.5.2 data evaluation software from WITec. All acquired spectra and hyperspectral scans were corrected for cosmic rays and the baseline was subtracted using a build-in background subtraction shape function of empirically optimized shape size of 500.

The hyperspectral scans were further processed using Python programming code for converting the Raman signal sampled in individual pixels into phasor space coordinates.

Spectral phasor analysis of Raman and fluorescence hyperspectral imaging data

The spectral phasor analysis of hyperspectral imaging data consists in calculating the real and imaginary components of the Fourier transform, respectively referred to as G and S, and using them as Cartesian coordinates on a 2D spectral phasor map. (G, S) are defined by the following expressions:

$$G = \frac{\int_{\lambda_0}^{\lambda_f} I(\lambda)\cos\left(\omega n(\lambda-\lambda_0)\right)\mathrm{d}\lambda}{\int_{\lambda_0}^{\lambda_f} I(\lambda)\mathrm{d}\lambda}, \quad \text{(M1)}$$

$$S = \frac{\int_{\lambda_0}^{\lambda_f} I(\lambda)\sin\left(\omega n(\lambda-\lambda_0)\right)\mathrm{d}\lambda}{\int_{\lambda_0}^{\lambda_f} I(\lambda)\mathrm{d}\lambda}, \quad \text{(M2)}$$

where $I(\lambda)$ for a particular pixel represents the intensity as a function of wavelength, measured in the interval $(\lambda_0; \lambda_f)$. This range depends on instrumental constraints and the type of detector used

for the analysis. In the present case the range 416–728 nm was used for ACDAN fluorescence data and the relevant truncated portions of the 2.6–8 µm spectral interval for Raman data. Note that changing the detection range will necessarily results in a change of the relative positions of different points on the phasor plot; therefore, the detection range must be conserved across all experiments in order to be able to compare measurements. The parameter n is the harmonic, i.e. the number of cycles of the trigonometric function that are fit in the wavelength range by means of the angular frequency ω:

$$\omega = \frac{2\pi}{(\lambda - \lambda_0)} \tag{M3}$$

When imaging with a microscope, we acquire a discrete number of spectral steps corresponding to the number of detection windows that cover the spectral range. For computational purposes, the spectral phasor transform is expressed as a discretized approximation of the continuous transform as:

$$G = \frac{\sum_c^{N_c} I(c)\cos(2\pi c/N_c)}{\sum_c^{N_c} I(c)}, \tag{M4}$$

$$S = \frac{\sum_c^{N_c} I(c)\sin(2\pi c/N_c)}{\sum_c^{N_c} I(c)}, \tag{M5}$$

where $I(c)$ is the pixel intensity at channel and c is the total number of channels. Conveniently, even if the total number of spectral acquisition channels is small (in our case 32 for fluorescence and over 200 for Raman), the coordinates S and G can be considered quasi-continuous, since the photon counts in each pixel and channel are high enough (>102) to allow a wide range of possible values of the coordinates S and G.

The spectral phasor approach obeys the rules of vector algebra, known as the linear combination of phasors. This property implies that a combination of two independent fluorescent species will appear on the phasor plot at a position that is a linear combination of the phasor positions of the two independent spectral species. The fraction of each component can be determined from the coefficients of the linear combination.

Note that the phase angle ϕ, and the modulation, M can be obtained through:

$$\phi = \arctan\left(\frac{S}{G}\right) \tag{M6}$$

$$M = \sqrt{S^2 + G^2} \tag{M7}$$

Geometric computation of fractional compositions based on phasor space coordinates

Using the spectral phasor coordinates of pure compounds, i.e. either lyophilized polymers or water (see Fig. S1b), the volume fraction occupied by a given compound in any given binary sample was computed according to

$$V_{phasor} = \frac{\sqrt{(G_{mix} - G_a)^2 + (S_{mix} - S_a)^2}}{\sqrt{(G_a - G_b)^2 + (S_a - S_b)^2}}. \tag{M8}$$

Here, subscripts “a”, “b” and “mix” respectively account for the reference pure compounds (i.e. polymer and water) and that of the mixture. Additionally, V_{phasor} quantifies the fraction of the

compound with subscript “b”, which is chosen arbitrarily as a notation for the given compound of interest.

A similar equation was used in the case of 3 pure compounds (see Fig. S1c). However, in such case, the point of coordinate (G_a, S_a) is taken as the intersection between the straight line connecting the data point of coordinates (G_D, S_D) and the pure compound of interest (G_b, S_b) with the straight line connecting the two other compounds of coordinates (G_c, S_c) and (G_d, S_d). The expression of the coordinates G_a and S_a for a 3-compound system consequently reads:

$$G_a = \frac{\frac{G_c - G_d}{S_c - S_d} G_c - \frac{G_{mix} - G_b}{S_{mix} - S_b} G_{mix} + S_{mix} - S_c}{\frac{G_c - G_d}{S_c - S_d} - \frac{G_{mix} - G_b}{S_{mix} - S_b}}, \quad \text{(M9)}$$

$$S_a = \frac{G_c - G_d}{S_c - S_d} (G_a - G_c) + S_c, \quad \text{(M10)}$$

ACKNOWLEDGEMENTS

A.M. acknowledges support from Alexander von Humboldt Foundation and CONICET. We acknowledge Nannan Chen for providing glycinin. We also acknowledge support from the German Academic Exchange Service (Deutscher Akademischer Austauschdienst, DAAD) in the framework of project 57654674. R.D. acknowledges the ComeInCell network funded by the European Union’s Horizon Europe research and innovation program under the Marie Skłodowska-Curie grant agreement No. 101168939.

REFERENCES

1. Pan, Y. et al. Small Molecules Influence the Physical Microenvironment of Biomolecular Condensates. *Journal of the American Chemical Society* (2025).
2. Ambadi Thody, S. et al. Small-molecule properties define partitioning into biomolecular condensates. *Nature Chemistry* **16**, 1794-1802 (2024).
3. Dai, Y. et al. Interface of biomolecular condensates modulates redox reactions. *Chem* **9**, 1594-1609 (2023).
4. Feric, M. et al. Coexisting liquid phases underlie nucleolar subcompartments. *Cell* **165**, 1686-1697 (2016).
5. Alberti, S. & Hyman, A.A. Biomolecular condensates at the nexus of cellular stress, protein aggregation disease and ageing. *Nature Reviews Molecular Cell Biology* **22**, 196-213 (2021).
6. Patel, A. et al. A liquid-to-solid phase transition of the ALS protein FUS accelerated by disease mutation. *Cell* **162**, 1066-1077 (2015).
7. Jawerth, L. et al. Protein condensates as aging Maxwell fluids. *Science* **370**, 1317-1323 (2020).
8. Ye, S. et al. Micropolarity governs the structural organization of biomolecular condensates. *Nature chemical biology* **20**, 443-451 (2024).
9. Villegas, J.A., Heidenreich, M. & Levy, E.D. Molecular and environmental determinants of biomolecular condensate formation. *Nature chemical biology* **18**, 1319-1329 (2022).
10. Zhu, L., Pan, Y., Hua, Z., Liu, Y. & Zhang, X. Ionic effect on the microenvironment of biomolecular condensates. *Journal of the American Chemical Society* **146**, 14307-14317 (2024).
11. Nakasako, M. Water–protein interactions from high–resolution protein crystallography. *Philosophical Transactions of the Royal Society of London. Series B: Biological Sciences* **359**, 1191-1206 (2004).
12. Best, R.B., Zheng, W. & Mittal, J. Balanced protein–water interactions improve properties of disordered proteins and non-specific protein association. *Journal of chemical theory and computation* **10**, 5113-5124 (2014).
13. Camino, J.D., Gracia, P. & Cremades, N. The role of water in the primary nucleation of protein amyloid aggregation. *Biophysical Chemistry* **269**, 106520 (2021).
14. Bellissent-Funel, M.-C. et al. Water determines the structure and dynamics of proteins. *Chemical reviews* **116**, 7673-7697 (2016).
15. Smolin, N., Oleinikova, A., Brovchenko, I., Geiger, A. & Winter, R. Properties of spanning water networks at protein surfaces. *The Journal of Physical Chemistry B* **109**, 10995-11005 (2005).
16. Thoke, H.S. et al. Tight coupling of metabolic oscillations and intracellular water dynamics in Saccharomyces cerevisiae. *PLoS One* **10**, e0117308 (2015).
17. Watson, J.L. et al. Macromolecular condensation buffers intracellular water potential. *Nature* **623**, 842-852 (2023).
18. Thoke, H.S., Thorsteinsson, S., Stock, R.P., Bagatolli, L.A. & Olsen, L.F. The dynamics of intracellular water constrains glycolytic oscillations in Saccharomyces cerevisiae. *Scientific Reports* **7**, 16250 (2017).

19. Vorontsova, I. et al. In vivo macromolecular crowding is differentially modulated by aquaporin 0 in zebrafish lens: Insights from a nanoenvironment sensor and spectral imaging. *Science Advances* **8**, eabj4833 (2022).
20. Duboué-Dijon, E., Fogarty, A.C., Hynes, J.T. & Laage, D. Dynamical disorder in the DNA hydration shell. *Journal of the American Chemical Society* **138**, 7610-7620 (2016).
21. Fogarty, A.C. & Laage, D. Water dynamics in protein hydration shells: the molecular origins of the dynamical perturbation. *The Journal of Physical Chemistry B* **118**, 7715-7729 (2014).
22. Laage, D., Elsaesser, T. & Hynes, J.T. Water dynamics in the hydration shells of biomolecules. *Chemical Reviews* **117**, 10694-10725 (2017).
23. Ghosh, R., Banerjee, S., Hazra, M., Roy, S. & Bagchi, B. Sensitivity of polarization fluctuations to the nature of protein-water interactions: Study of biological water in four different protein-water systems. *The Journal of Chemical Physics* **141** (2014).
24. Dai, Y., You, L. & Chilkoti, A. Engineering synthetic biomolecular condensates. *Nature Reviews Bioengineering* **1**, 466-480 (2023).
25. Visser, B.S., Lipiński, W.P. & Spruijt, E. The role of biomolecular condensates in protein aggregation. *Nature Reviews Chemistry* **8**, 686-700 (2024).
26. Boija, A., Klein, I.A. & Young, R.A. Biomolecular condensates and cancer. *Cancer cell* **39**, 174-192 (2021).
27. Spruijt, E., Westphal, A.H., Borst, J.W., Cohen Stuart, M.A. & van der Gucht, J. Binodal compositions of polyelectrolyte complexes. *Macromolecules* **43**, 6476-6484 (2010).
28. Abbas, M., Lipiński, W.P., Nakashima, K.K., Huck, W.T. & Spruijt, E. A short peptide synthon for liquid–liquid phase separation. *Nature Chemistry* **13**, 1046-1054 (2021).
29. Smokers, I.B. et al. Selective ion binding and uptake shape the microenvironment of biomolecular condensates. *Journal of the American Chemical Society* **147**, 25692-25704 (2025).
30. Sabri, E., Mangiarotti, A. & Dimova, R. Fluorescence-based mapping of condensate dielectric permittivity uncovers hydrophobicity-driven membrane interactions. *bioRxiv*, 2025.2003.2009.642144 (2025).
31. Butler, H.J. et al. Using Raman spectroscopy to characterize biological materials. *Nature protocols* **11**, 664-687 (2016).
32. Pezzotti, G. Raman spectroscopy in cell biology and microbiology. *Journal of Raman Spectroscopy* **52**, 2348-2443 (2021).
33. Dodo, K., Fujita, K. & Sodeoka, M. Raman spectroscopy for chemical biology research. *Journal of the American Chemical Society* **144**, 19651-19667 (2022).
34. Kuhar, N., Sil, S., Verma, T. & Umapathy, S. Challenges in application of Raman spectroscopy to biology and materials. *RSC advances* **8**, 25888-25908 (2018).
35. Vardaki, M.Z., Gregoriou, V.G. & Chochos, C.L. Biomedical applications, perspectives and tag design concepts in the cell–silent Raman window. *RSC Chemical Biology* **5**, 273-292 (2024).
36. Hansen, P.E., Vakili, M., Kamounah, F.S. & Spanget-Larsen, J. NH stretching frequencies of intramolecularly hydrogen-bonded systems: an experimental and theoretical study. *Molecules* **26**, 7651 (2021).
37. Avni, A., Joshi, A., Walimbe, A., Pattanashetty, S.G. & Mukhopadhyay, S. Single-droplet surface-enhanced Raman scattering decodes the molecular determinants of liquid-liquid phase separation. *Nature Communications* **13**, 4378 (2022).

38. Mangiarotti, A. et al. Biomolecular condensates modulate membrane lipid packing and hydration. *Nature Communications* **14**, 6081 (2023).
39. Shibuya, R. et al. Nucleic acid-rich stress granules are not merely crowded condensates: A quantitative Raman imaging study. *Analytical Chemistry* **96**, 17078-17085 (2024).
40. Madhu, M., Santhoshkumar, S., Tseng, W.-B. & Tseng, W.-L. Maximizing analytical precision: exploring the advantages of ratiometric strategy in fluorescence, Raman, electrochemical, and mass spectrometry detection. *Frontiers in Analytical Science* **3**, 1258558 (2023).
41. Joshi, A. et al. Hydrogen-bonded network of water in phase-separated biomolecular condensates. *The Journal of Physical Chemistry Letters* **15**, 7724-7734 (2024).
42. Ibrahim, K.A., Naidu, A.S., Miljkovic, H., Radenovic, A. & Yang, W. Label-free techniques for probing biomolecular condensates. *ACS nano* **18**, 10738-10757 (2024).
43. Tobita, R. et al. Highly sensitive Raman measurements of protein aqueous solutions using liquid–liquid phase separation. *Chemical Communications* **60**, 8732-8735 (2024).
44. Mangiarotti, A. & Bagatolli, L.A. Impact of macromolecular crowding on the mesomorphic behavior of lipid self-assemblies. *Biochimica et Biophysica Acta (BBA)-Biomembranes* **1863**, 183728 (2021).
45. Liu, Y., Lipowsky, R. & Dimova, R. Concentration dependence of the interfacial tension for aqueous two-phase polymer solutions of dextran and polyethylene glycol. *Langmuir* **28**, 3831-3839 (2012).
46. Malacrida, L., Ranjit, S., Jameson, D.M. & Gratton, E. The phasor plot: a universal circle to advance fluorescence lifetime analysis and interpretation. *Annual review of biophysics* **50**, 575-593 (2021).
47. van Haren, M.H., Visser, B.S. & Spruijt, E. Probing the surface charge of condensates using microelectrophoresis. *Nature Communications* **15**, 3564 (2024).
48. Patel, A. et al. ATP as a biological hydrotrope. *Science* **356**, 753-756 (2017).
49. Saurabh, S. et al. ATP-responsive biomolecular condensates tune bacterial kinase signaling. *Science Advances* **8**, eabm6570 (2022).
50. Ahlers, J. et al. The key role of solvent in condensation: Mapping water in liquid-liquid phase-separated FUS. *Biophysical journal* **120**, 1266-1275 (2021).
51. Shiraga, K., Ogawa, Y. & Kondo, N. Hydrogen bond network of water around protein investigated with terahertz and infrared spectroscopy. *Biophysical journal* **111**, 2629-2641 (2016).
52. Bannon, S.M. et al. Characterizing Hydrated Polymers via Dielectric Relaxation Spectroscopy: Connecting Relative Permittivity, State of Water, and Salt Transport Properties of Sulfonated Polysulfones. *Macromolecules* (2025).
53. De Luca, G., Malacrida, L., Vetri, V. & Sancataldo, G. Unveiling water ordering in liquid-liquid phase separation using bovine serum albumin-polyethylene glycol systems. *Journal of Molecular Liquids*, 127865 (2025).
54. Teo, W. et al. Nile Red fluorescence spectroscopy reports early physicochemical changes in myelin with high sensitivity. *Proceedings of the National Academy of Sciences* **118**, e2016897118 (2021).
55. Romero-Perez, P.S., Dorone, Y., Flores, E., Sukenik, S. & Boeynaems, S. When phased without water: biophysics of cellular desiccation, from biomolecules to condensates. *Chemical reviews* **123**, 9010-9035 (2023).
56. Lakowicz, J.R. Principles of fluorescence spectroscopy. (Springer, 2006).

57. Stadler, C. et al. Immunofluorescence and fluorescent-protein tagging show high correlation for protein localization in mammalian cells. *Nature methods* **10**, 315-323 (2013).
58. Kocaoglu, O. & Carlson, E.E. Progress and prospects for small-molecule probes of bacterial imaging. *Nature chemical biology* **12**, 472-478 (2016).
59. Götzke, H. et al. The ALFA-tag is a highly versatile tool for nanobody-based bioscience applications. *Nature communications* **10**, 4403 (2019).
60. King, M.R. et al. Macromolecular condensation organizes nucleolar sub-phases to set up a pH gradient. *Cell* **187**, 1889-1906. e1824 (2024).
61. Dragwidge, J.M. et al. Biomolecular condensation orchestrates clathrin-mediated endocytosis in plants. *Nature Cell Biology* **26**, 438-449 (2024).
62. Bussi, C. et al. Stress granules plug and stabilize damaged endolysosomal membranes. *Nature* **623**, 1062-1069 (2023).
63. Chen, N., Zhao, Z., Wang, Y. & Dimova, R. Resolving the mechanisms of soy glycinin self-coacervation and hollow-condensate formation. *ACS macro letters* **9**, 1844-1852 (2020).
64. Aggarwal, S. et al. Myelin membrane assembly is driven by a phase transition of myelin basic proteins into a cohesive protein meshwork. *PLoS biology* **11**, e1001577 (2013).
65. Mangiarotti, A., Chen, N., Zhao, Z., Lipowsky, R. & Dimova, R. Wetting and complex remodeling of membranes by biomolecular condensates. *Nature communications* **14**, 2809 (2023).